pubs.acs.org/Biomac

Article

Embedding Collagen in Multilayers for Enzyme-Assisted Mineralization: A Promising Way to Direct Crystallization in Confinement

Elodie Colaço, Clément Guibert, Jihye Lee, Emmanuel Maisonhaute, Dalil Brouri, Christine Dupont-Gillain, Karim El Kirat, Sophie Demoustier-Champagne, and Jessem Landoulsi*

Cite This: *Biomacromolecules* 2021, 22, 3460−3473

Read Online

ACCESS | Metrics & More | Article Recommendations | Supporting Information

ABSTRACT: The biogenic calcium phosphate (CaP) crystallization is a process that offers elegant materials design strategies to achieve bioactive and biomechanical challenges. Indeed, many biomimetic approaches have been developed for this process in order to produce mineralized structures with controlled crystallinity and shape. Herein, we propose an advanced biomimetic approach for the design of ordered hybrid mineralized nano-objects with highly anisotropic features. For this purpose, we explore the combination of three key concepts in biomineralization that provide a unique environment to control CaP nucleation and growth: (i) self-assembly and self-organization of biomacromolecules, (ii) enzymatic heterogeneous catalysis, and (iii) mineralization in confinement. We use track-etched templates that display a high density of aligned monodisperse pores so that each nanopore may serve as a miniaturized mineralization bioreactor. We enhance the control of the crystallization in these systems by coassembling type I collagen and enzymes within the nanopores, which allows us to tune the main characteristics of the mineralized nano-objects. Indeed, the synergy between the gradual release of one of the mineral ion precursors by the enzyme and the role of the collagen in the regulation of the mineralization allowed to control their morphology, chemical composition, crystal phase, and mechanical stability. Moreover, we provide clear insight into the prominent role of collagen in the mineralization process in confinement. In the absence of collagen, the fraction of crystalline nano-objects increases to the detriment of amorphous ones when increasing the degree of confinement. By contrast, the presence of collagen-based multilayers disturbs the influence of confinement on the mineralization: platelet-like crystalline hydroxyapatite form, independently of the degree of confinement. This suggests that the incorporation of collagen is an efficient way to supplement the lack of confinement while reinforcing mechanical stability to the highly anisotropic materials. From a bioengineering perspective, this biomineralization-inspired approach opens up new horizons for the design of anisotropic mineralized nano-objects that are highly sought after to develop biomaterials or tend to replicate the complex structure of native mineralized extracellular matrices.

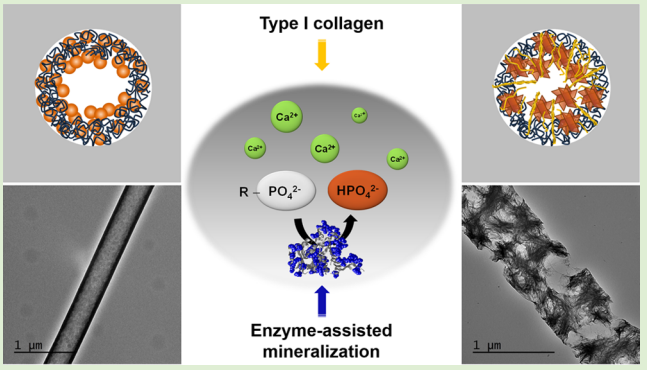

1. INTRODUCTION

In vivo, cells evolve in a complex environment regarding physiological conditions, biochemical signals, organization at macro-/nanoscale and mechanical properties.[1,2] The design of biointerfaces able to recreate the conditions ultimately guiding cell fate, and originally provided by the extracellular matrix (ECM), has been increasingly recognized as the "key to the success" for the control of cell−material interactions.[3] In hard mineralized tissues of vertebrates, such as in bone, tooth (dentine), and mineralized cartilage, in addition to the three-dimensional network of fibrillary proteins and other biomacromolecules, the ECM includes a mineral phase, typically calcium phosphate (CaP), organized in a structural hierarchy with the soft matter.[4] During the past decade, many efforts have been devoted to the development of materials replicating the composition of native mineralized ECMs. The synthesis of hybrid materials, including both hard mineral and soft bio-organic phases, was, indeed, proposed as a promising option to overcome this challenge. The main advantages of hybrid materials lie in their versatility, and the possibility to tune their chemical composition, bioactivity, and mechanical properties.[5−7] In the context of biomineralization, this concept has

Received: May 3, 2021
Revised: June 16, 2021
Published: July 7, 2021

https://doi.org/10.1021/acs.biomac.1c00565
Biomacromolecules 2021, 22, 3460−3473

led to the publication of numerous procedures which can be roughly divided into three categories: (i) mineralization in homogeneous phase of type I collagen,[8] often with the addition of synthetic polymers;[9] (ii) mineralization of adsorbed collagen layers or collagen matrices, that is, in the heterogeneous phase,[10,11] and (iii) assembly of collagen and synthesized CaP nanoparticles.[12] These procedures have led to the elaboration of a rich and fascinating repertoire of hybrid nanostructures, which has extended their use in broad biomedical applications.[13] They also showed that collagen plays a pivotal role in the mineralization process. Collagen fibrils are, indeed, considered as the key site where CaP nucleates, yielding what is called "intrafibrillar mineralization",[10,11,14−16] and offer to the mineral a suitable environment for its growth. Moreover, it must be kept in mind that type I collagen exhibits a strong affinity to noncollagenous proteins, such as bone sialoprotein and osteopontin, which are key actors in the regulation of the mineralization process.[17,18]

Although the chemical environment of the ECM provided by biomacromolecules, including collagen and noncollagenous proteins, regulates the formation of the mineral, it does not guarantee the control of the morphology of the crystals. It seems that organisms exploit confinement to this end.[19,20] At the nanoscale, confinement may, indeed, impact the crystal properties, the nucleation, and the growth mechanism.[21] These effects can be explained by the critical size concept invoked by classical nucleation theory and the competitive balance between surface and volume free energies: under confinement, the particle size is reduced; hence, the surface area-to-volume ratio of the particles increases. These considerations are particularly important for polymorph crystals, such as CaP, as confinement may influence the size-dependent polymorphism.

Combining the use of confinement with chemical environment, typically type I collagen appears clearly as a relevant strategy for the control of the mineral phase, and thus the elaboration of hybrid mineralized nanostructures. However, the control of nucleation in confinement, without being disturbed by bulk mineralization, is challenging.[22] To overcome this difficulty, mineralization may be initiated by generating, in situ, CaP ion precursors through an enzyme-catalyzed reaction, similar to the process adopted by live organisms. This idea has motivated the use of enzymes for the development of biomimetic systems, which may help to better understand the mechanism of biomineralization,[23,24] or for the design of biomaterials.[25−27] In recent works, we have used tissue nonspecific alkaline phosphatase (ALP, EC 3.1.3.1) to initiate CaP mineralization in the homogeneous phase by generating, in situ, orthophosphate ions, which precipitate in the presence of calcium ions.[28] This procedure was also successfully applied on solid surfaces, using immobilized enzymes, resulting in the formation of nanostructured mineralized layers.[29] Interestingly, we observed that the degree of confinement influences the crystal phase. These findings suggest that the enzyme-assisted mineralization, through a heterogeneous catalysis approach, is a powerful way to control the CaP nucleation in space and in time, likewise the mechanism by which organisms regulate mineralization.

In the present paper, we propose an advanced biomimetic approach for the design of ordered hybrid mineralized nanostructures with anisotropic features. To modulate their characteristics, in terms of morphology, dimensions, chemical composition, and crystallinity, we combine (i) the sequential layer-by-layer (LbL) assembly method, (ii) the enzyme-assisted mineralization, and (iii) the template-based synthesis. This approach provides a favorable environment to control CaP nucleation and growth. The biomimicry is developed here at three different levels. First, the incorporation of collagen, the main protein of hard mineralized tissues of vertebrates, offers a suitable chemical environment. Second, the nucleation of the mineral phase is initiated by means of in situ-controlled generation of CaP precursor via an enzyme-assisted process, thus, mimicking the way by which matrix vesicles generate a mineral in the extracellular space.[30,31] Third, the whole process takes place in a nanoscale confined medium using track-etched templates, which provides a high density of aligned monodisperse pores, so that each nanopore may serve as a miniaturized mineralization bioreactor.

2. EXPERIMENTAL SECTION

2.1. Materials. Poly(allylamine hydrochloride) (PAH, $M_w \sim 17$ kDa), poly(4-styrenesulfonic acid) sodium salt (PSS, $M_w \sim 70$ kDa), poly(acrylic acid) (PAA, $M_w \sim 15$ kDa), calcium chloride ($CaCl_2$, ≥99%), sodium chloride (NaCl, ≥99%), α-glycerol phosphate magnesium salt hydrate (~85%), *N*-(3-(dimethylamino)propyl)-*N*′-ethylcarbodiimide hydrochloride (EDC), *N*-hydroxysuccinimide (NHS, ≥98%), 4-nitrophenyl phosphate disodium salt hexahydrate (pnpp, ≥99%), and 4-nitrophenol (pnp) were purchased from Sigma-Aldrich (France). Dichloromethane (CH_2Cl_2, ≥99.5%) and hydrochloric acid (HCl, 37%) were purchased from VWR (France) and sodium hydroxide 9.31 N (NaOH) from Volusol (U.S./Canada). Alkaline phosphatase from bovine intestinal mucosa (ALP, ≥10 U/mg) was purchased from Sigma-Aldrich (France). Type I collagen G from bovine calf skin (Col, 4 mg/mL) was purchased from Biochrom GmbH (Germany). Sodium hyaluronate (HA, $M_w \sim 151-300$ kDa) was purchased from Lifecore Biomedical (U.S.A.). All aqueous solutions were prepared in ultrapure water (Milli-Q, Millipore, France) and the pH was adjusted by addition of HCl 0.1 M or NaOH 0.1 M.

2.2. Electrophoretic Mobility (EPM). EPM measurements were carried out in solutions of type I collagen (Col), alkaline phosphatase (ALP), and sodium hyaluronate (HA) using a Malvern Zetasizer nanoZS with disposable polystyrene cuvettes (DTS1061, Malvern Instruments Ltd., U.K.). The calibration of the instrument was checked using an EPM transfer standard polystyrene latex solution (DTS1235, Malvern). The obtained results correspond to the means of five replicates.

2.3. Mineralization in Solution. A solution of $CaCl_2$ (11.4 mM) was prepared in ultrapure water. α-Glycerol phosphate was then added to get a final concentration of 7 mM. ALP was subsequently introduced at a final concentration of 0.1 mg/mL. The solution was finally adjusted to pH 7.4 and the mixture was gently stirred for 48 h at 37 °C, producing a precipitate. It was then centrifuged, washed three times with ultrapure water, and allowed to dry under air.

2.4. LbL Assemblies and Mineralization on a Planar Surface.

2.4.1. In Situ Monitoring. LbL assemblies and subsequent mineralization were performed on a planar surface and monitored in situ using a quartz crystal microbalance with dissipation monitoring (QCM-D). Unless stated elsewhere, measurements were operated at 37 °C using a Q-Sense E4 System (Sweden). The adsorption of the macromolecules was performed on sensors coated with a thin layer of SiO_2 provided by Q-Sense. The sensors were cleaned by UV-ozone for 15 min and rinsed with ethanol before measurement. Oscillation of the quartz crystal at the resonant frequency (5 MHz) or at one of its overtones (15, 25, 35, 45, 55, and 65 MHz) was obtained by applying an ac voltage. The evolution of the resonance frequency (Δf) and of dissipation (ΔD) was monitored upon adsorption of the different components. Solutions were injected into the cells using a peristaltic pump (Ismatec IPC-N 4) at a flow rate of 50 μL/min.

(PAH/ALP)$_5$ Multilayers. Prior to the multilayer buildup, water adjusted to pH 7.4 was used to establish the baseline. First, PAH solution (1 mg/mL) adjusted to pH 7.4 was brought into the

https://doi.org/10.1021/acs.biomac.1c00565
Biomacromolecules 2021, 22, 3460−3473

Scheme 1. Procedures Used for the Design of Ordered Mineralized Nano-Objects with Highly Anisotropic Features[a]

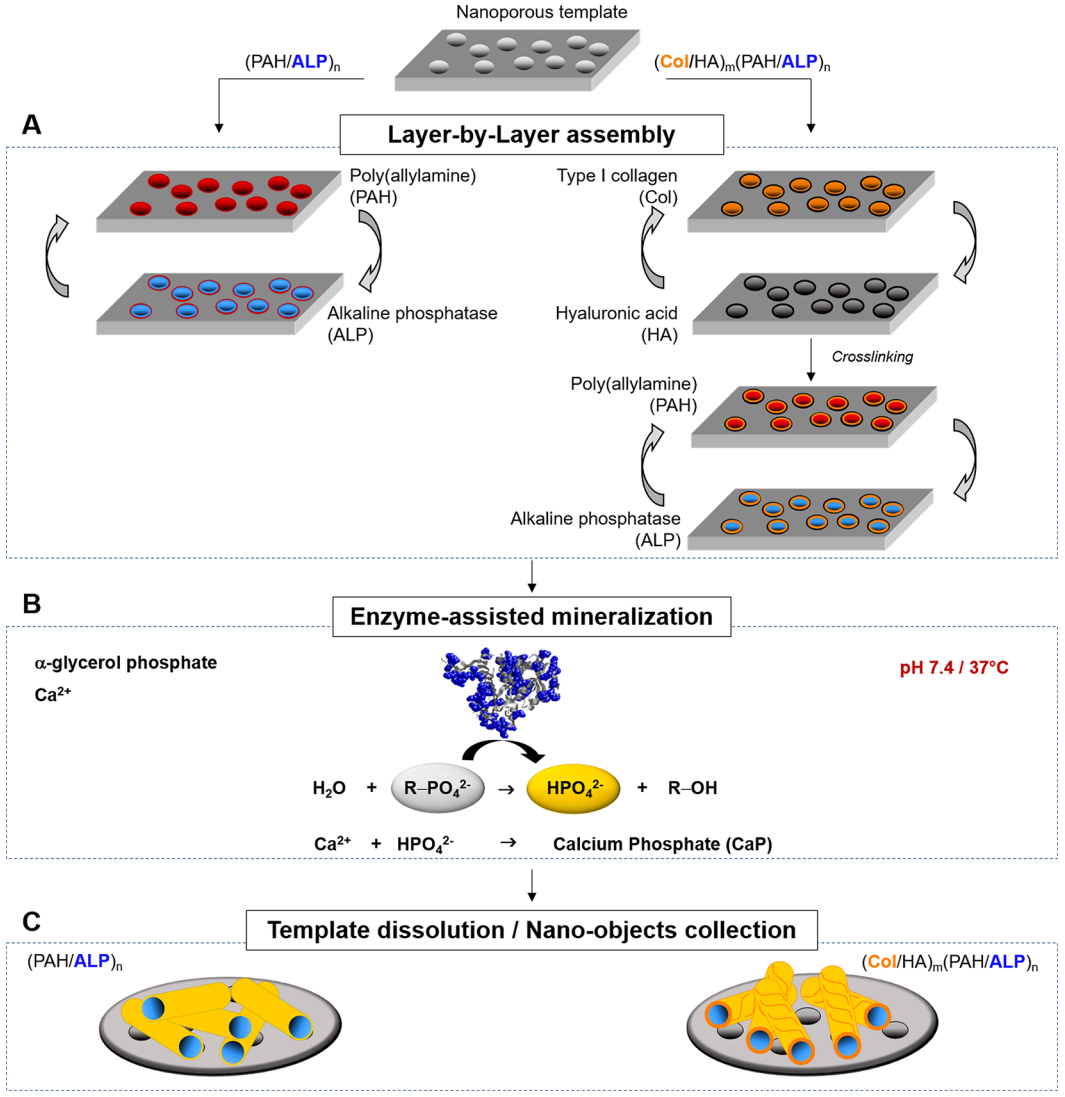

[a](A) Sequential layer-by-layer assembly of $(PAH/ALP)_n$ (left) and $(Col/HA)_m(PAH/ALP)_n$ (right) multilayers by alternate immersion of a nanoporous template (track-etched polycarbonate membrane) in the different solutions, as indicated. (B) Initiation of the enzyme-assisted mineralization by incubating the functionalized templates in aqueous solution containing Ca^{2+} ions and α-glycerol phosphate, the substrate of ALP, that is converted into orthophosphate via the enzyme-catalyzed reaction, yielding the calcium phosphate (CaP) mineral. (C) Dissolution of the template and collection of the mineralized $(PAH/ALP)_n$ (left) and $(Col/HA)_m(PAH/ALP)_n$ (right) nano-objects by filtration through a PET track-etched membrane.

measurement cell over a period of 10 min, followed by a rinsing step with water at pH 7.4 for 10 min. PAA solution (1 mg/mL) at pH 7.4 was then brought into the measurement cell for 10 min and rinsed for 10 min with water at pH 7.4 to build up an anchoring layer. Then, PAH and ALP (0.1 mg/mL) solutions were alternately injected during 10 and 30 min, respectively.

$(Col/HA)_3(PAH/ALP)_5$ Multilayers. Prior to the buildup of multilayers, a water solution (pH 4.5) was used to establish the baseline at RT. First, PAH solution (1 mg/mL) at pH 4.5 was injected for 10 min, then the cells were rinsed with water at pH 4.5 for 10 min. Subsequently, PSS solution (1 mg/mL) at pH 4.5 was brought into the measurement cell for 10 min and rinsed for 10 min with ultrapure water at pH 4.5. This first bilayer corresponds to an anchoring layer. Then, Col (0.1 mg/mL) and HA (1 mg/mL) solutions, prepared in water at pH 4.5, were alternately injected for 30 and 10 min, respectively. After the construction of three bilayers, $(Col/HA)_3$, a cross-linking solution (EDC 30 mM, NHS 50 mM) was injected into the cell overnight, following the procedure adapted from a previous study.[32] A rinsing step in ultrapure water at pH 7.4 was applied and the temperature fixed at 37 °C. Then, PAH (1 mg/mL) and ALP (0.1 mg/mL) solutions in water at pH 7.4 were alternately injected for 10 and 30 min, respectively, up to the buildup of five bilayers, $(PAH/ALP)_5$.

Mineralization. After the buildup of $(PAH/ALP)_5$ or $(Col/HA)_3(PAH/ALP)_5$ multilayers and subsequent rinsing, the mineralization was initiated by injecting a solution (pH 7.4) containing $CaCl_2$ (11.4 mM) and α-glycerol phosphate (7 mM) at 37 °C overnight.

2.4.2. Ex Situ Characterizations. For ex situ characterizations, the buildup of $(PAH/ALP)_5$ or $(Col/HA)_3(PAH/ALP)_5$ multilayers and subsequent mineralization were performed on a silicon wafer (⟨100⟩, Sigma-Aldrich) cleaned prior to use in a piranha solution (H_2SO_4 (96%)/H_2O_2 (30%) 1/3 v/v) for 30 min then rinsed with ultrapure water and dried under a nitrogen flow. The procedure of assembly was similar to the one described for in situ monitoring. Mineralization was performed in a Petri dish containing a mixture of $CaCl_2$ (11.4 mM) and α-glycerol phosphate (7 mM) solutions placed in the oven (37 °C) for 48 h without stirring. Samples were then rinsed in

https://doi.org/10.1021/acs.biomac.1c00565
Biomacromolecules 2021, 22, 3460−3473

ultrapure water and dried for ex situ characterizations using atomic force microcopy (AFM) and scanning electron microscopy (SEM).

2.5. LbL Assemblies and Mineralization in Nanoporous Templates. The buildup of $(PAH/ALP)_5$ and $(Col/HA)_3(PAH/ALP)_5$ multilayers was performed at 37 °C, by immersing alternately a 25 μm thick polycarbonate (PC) membrane (1 cm × 1 cm) with pore size of 200 (ø = 204.9 ± 14.4 nm) or 500 nm (ø = 495.4 ± 15.8 nm) and pore density of 1×10^8 pores·cm^{-2} provided by It4ip (Louvain-la-Neuve, Belgium) in the different solutions, following the procedure described for planar surfaces, except that the immersion time was 30 min for polyelectrolytes and biomacromolecules (Scheme 1A). The membrane was rinsed in two water baths for 2 min between each layer deposition. After the LbL assembly, the top and bottom surfaces of the membranes were decrusted with a cotton swab immersed in a solution of NaCl 3 M (pH 12) and then rinsed in water. The membranes were subsequently incubated in the mineralization solution at pH 7.4 ($CaCl_2$ 11.4 mM, α-glycerol phosphate 7 mM) for 48 h at 37 °C (Scheme 1B). A rinsing step was then carried out in two different baths (2 min each) of water. The membranes were subsequently dried under a nitrogen flow.

2.6. Atomic Force Microscopy (AFM). AFM images were recorded using a commercial AFM (NanoScope VIII MultiMode AFM, Bruker Nano Inc., Nano Surfaces Division, Santa Barbara, CA.). The substrates were fixed on a steel sample puck using a small piece of adhesive tape. Images were recorded in ambient conditions at room temperature (~22 °C) using oxide-sharpened microfabricated Si_3N_4 cantilevers (SNL-10, Bruker Nano Inc., Nano Surfaces Division, Santa Barbara, CA.).

2.7. Transmission Electron Microscopy (TEM). TEM micrographs were acquired using a JEOL JEM-2100F instrument, equipped with a CCD camera, at an acceleration voltage of 200 kV. The PC membrane with embedded nanotubes was dissolved in 3 mL of dichloromethane, and the nanotubes were collected on a copper mesh grid coated with an amorphous carbon film (Scheme 1C). The elemental content of the nanotubes was identified using energy-dispersive X-ray spectroscopy (EDX) measurements in scanning transmission electron microscopy (STEM) mode, and their crystallinity was assessed using selected area electron diffraction (SAED).

2.8. Scanning Electron Microscopy (SEM). Mineralized multilayers were imaged by scanning electron microscope (SEM, FEI Quanta FEC 250) at an acceleration voltage operating at 10−20 kV. After rinsing in three water baths at pH 7.4 and subsequent drying under nitrogen gas, samples were metallized by gold sputtering for a better image contrast. For the mineralized nano-objects, the PC membrane, used as a template, was dissolved in 3 mL of dichloromethane and filtrated through a 23 μm thick poly(ethylene terephthalate) (PET) membrane of 200 nm average pore size provided by It4ip to entrap the liberated nanotubes, rinsed with dichloromethane and then dried under vacuum.

3. RESULTS AND DISCUSSION

3.1. Properties of the Biomacromolecules in Solution. Type I collagen is made of three left-handed helical polypeptide chains (two α1 and one α2) with nonhelical ends (telopeptides) entwined in a superhelix with molecular dimensions of ~300 nm in length and ~1.5 nm in diameter. The evolution of the net charge of collagen (Col) as a function of the pH was investigated by EPM with a view of incorporating them in LbL assemblies (Figure 1A). Results revealed that the collagen is negatively charged for pH values ranging from 6 to 12 and positively charged at pH below 5, suggesting that the isoelectric point (iep) of the macromolecule is between 6 and 7. However, the collagen molecule has a particular charge distribution due to its highly anisotropic structure. Its iep is then not well-defined, and divergent experimental values of 6.0 and 9.3 were reported in the literature.[33−35] The theoretical iep, computed using the amino

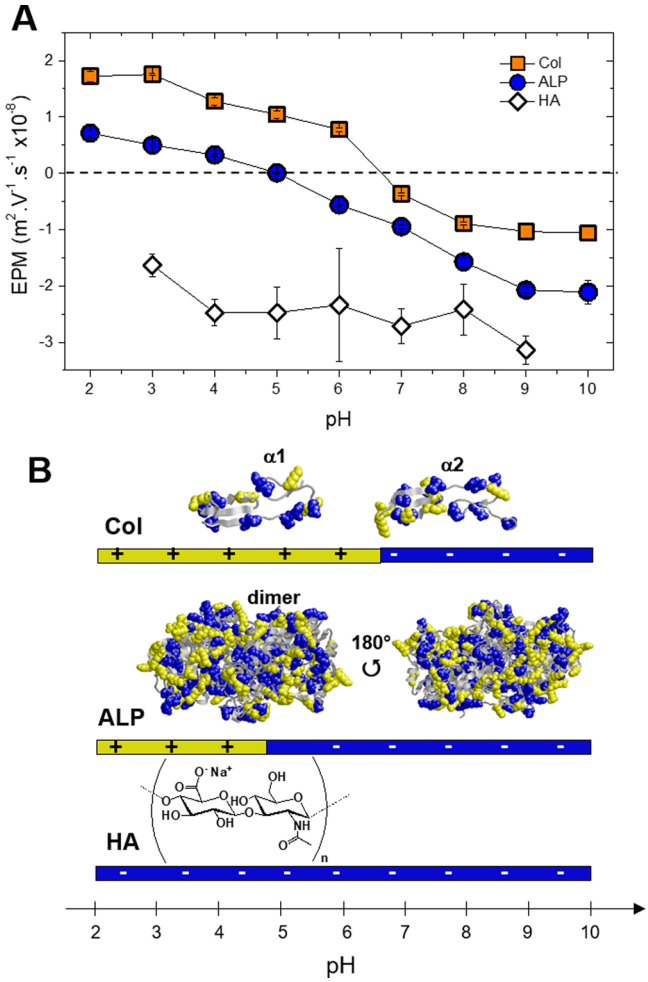

Figure 1. (A) Evolution of the electrophoretic mobility (EPM) as a function of pH of the biomacromolecules used in layer-by-layer assemblies: collagen (Col), alkaline phosphatase (ALP), and hyaluronic acid (HA). (B) Three-dimensional and molecular structures of the studied biomacromolecules and their overall surface charge as a function of the pH. (Col: α1 and α2 chains, PDB, code "P02453" and "P02459" respectively) constituting collagen triple-helix; ALP: two views of a homodimer related by a 180° rotation (PDB, code "P19111"). The superimposed residues Glu/Asp (in blue) and Arg/Lys (in yellow) are shown.

acid composition of α1 and α2 collagen chains, on the basis of the ProtParam tool, gives a value close to 9.[36] The discrepancies observed in the iep of collagen probably originate from the collagen source and preparation procedures which strongly impact the composition of telopeptides. More importantly, the notion of iep for collagen is questionable, owing to its highly anisotropic structure, possibly resulting in a heterogeneous charge distribution along the triple-helix (see charged residues in α1 and α2 chains, Figure 1B). This feature makes the integration of collagen in LbL assemblies difficult, particularly at physiological pH value. Indeed, collagen-based multilayers have been achieved only in acidic media[37−40] where collagen behaves as a polycation, which appears to be unrealizable near physiological pH values.[41] As for HA, it is negatively charged over the whole studied pH range (Figure 1A): Col/HA LbL assemblies could then be formed, below pH 6 (Figure 1B), in agreement with previous reports.[38,39]

A similar EPM profile was observed for ALP with a shift toward lower pH values and an iep around 5, suggesting that

https://doi.org/10.1021/acs.biomac.1c00565
Biomacromolecules 2021, 22, 3460−3473

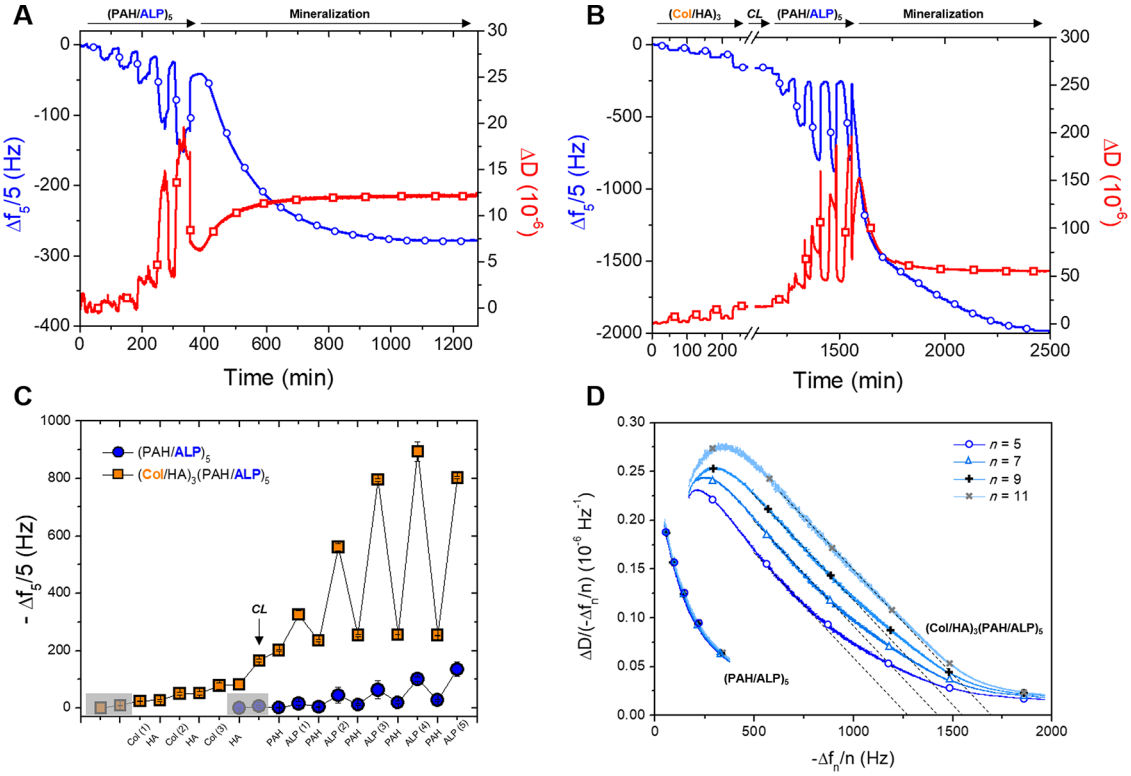

Figure 2. In situ monitoring of layer-by-layer assemblies and enzyme-assisted mineralization on planar surface. (A, B) QCM-D measurements showing frequency changes in the 5th overtone and the corresponding dissipation during the buildup of (A) $(PAH/ALP)_5$ (pH 7.4; 37 °C) and (B) $(Col/HA)_3(PAH/ALP)_5$ multilayers (pH 4.5; RT) and cross-linking (CL), followed by mineralization (pH 7.4; 37 °C). (C) Evolution of the frequency shift, taken at the 5th overtone, as a function of the number of deposited layers (gray shaded areas correspond to the anchoring layers, and the arrow indicates cross-linking, CL, after the buildup of $(Col/HA)_3$ multilayers). (D) Typical evolution of $\Delta D/-\Delta f$ as a function of $-\Delta f$ corresponding to the mineralization process after the buildup of $(PAH/ALP)_5$ and $(Col/HA)_3(PAH/ALP)_5$ multilayers in the same studied condition (pH 7.4, 37 °C) at different overtones (n = 5, 7, 9, 11). Dashed lines correspond to linear regression fits to the data.

ALP exhibits an overall negatively charged surface at physiological pH. Indeed, as we reported previously,[29] this value is consistent with calculations through Protparam, when taking into account the amino acid composition of the enzyme (see the charged residues in Figure 1B). By contrast, it is well established that PAH displays an iep between 8 and 9[42] and is thus positively charged at physiological pH. Both ALP and PAH can then be and stay assembled into PAH/ALP multilayers through a LbL process at physiological pH (see Figure 1B).

Assembling both kinds of multilayers, Col/HA and PAH/ALP, in a single film is then impossible at physiological pH since Col/HA should not be stable at physiological pH. In order to overcome this obstacle, the first Col/HA assembly prepared at pH 4.5 was further cross-linked with EDC and NHS. The so-obtained consolidated multilayer assembly was shown to display an enhanced stability.[43] This increased robustness allows then to change the pH and proceed to the PAH/ALP multilayer formation at pH 7.4.

The catalytic activity of ALP was assessed in solution in the studied conditions (pH 7.4, 37 °C). Results show that the concentration of pnp, the product of the enzymatic reaction, increased progressively with the ALP concentration in solution (Figure S1A, Supporting Information). A linear relationship was obtained between the initial activity and ALP concentration at values ranging from 0.01 to 0.1 mg/mL (Figure S1B).

3.2. LbL Assemblies and Mineralization on Planar Surfaces. The incorporation of collagen and enzymes in a multilayered film and the mechanism of mineralization are first investigated on planar surfaces. The buildup of $(PAH/ALP)_n$ and $(Col/HA)_m(PAH/ALP)_n$ multilayers (where n and m represent the number of deposited ALP- and Col-based bilayers, respectively) was monitored in situ by QCM-D. Figure 2A shows the typical evolution of the resonance frequency (Δf) and dissipation (ΔD) shifts due to the alternate adsorption of PAH and ALP, indicating that these macromolecules assemble in a multilayered film, in agreement with previous findings.[29] Owing to the considerations described above (see section 3.1), related to the EPM behavior of the different biomacromolecules, the incorporation of collagen in polyelectrolyte multilayers was made possible in acidic media by using HA as a polyanion: the buildup of $(Col/HA)_m$ multilayers was, thus, carried out at pH 4.5. The evolution of Δf and ΔD signals confirms the buildup of $(Col/HA)_3$ multilayers (Figure S2A, Supporting Information). The obtained multilayers were then submitted to cross-linking treatment to prevent their degradation upon immersion near physiological conditions. Subsequently, LbL assembly of $(PAH/ALP)_5$ multilayers was performed over the cross-linked $(Col/HA)_3$ multilayers and monitored, in situ, by means of QCM-D. Results, given in Figure 2B, show changes in Δf and ΔD signals, which are similar to the ones observed for $(PAH/ALP)_n$ system. A noticeable increase in the frequency and decrease of the dissipation are observed for each injection of

https://doi.org/10.1021/acs.biomac.1c00565
Biomacromolecules 2021, 22, 3460−3473

ALP into the QCM-D cell, while the addition of PAH induces an opposite trend, which may be explained by a partial desorption of macromolecules (Figure S2B, Supporting Information). This behavior strongly impacts the growth mechanism of $(PAH/ALP)_n$ multilayers, as shown more clearly by the sawtoothed pattern in the Δf versus n plots (Figure 2C), and is independent of the presence of the underlying cross-linked $(Col/HA)_3$ multilayers. Sawtoothed patterns are, indeed, observed for the two studied systems: $(PAH/ALP)_n$ and $(Col/HA)_m(PAH/ALP)_n$ (respectively, blue disks and orange squares in Figure 2C). However, in the latter case, the magnitude of Δf variations is considerably higher (ca. 500 Hz compared to ca. 100 Hz). This trend may be explained by the loss of film stiffness during multilayer growth, as shown by the high dissipation values (variations around 100×10^{-6} for $(Col/HA)_3(PAH/ALP)_5$ versus variations around 10×10^{-6} for $(PAH/ALP)_n$; Figure 2A,B). These observations support the formation of softer multilayers, presumably with a higher hydration rate, for $(Col/HA)_3(PAH/ALP)_5$ systems, directly connected to the intrinsic properties of HA and Col and their organization at the solid/liquid interface under physiological conditions.

After the construction of $(PAH/ALP)_5$ and $(Col/HA)_3(PAH/ALP)_5$ multilayers, the mineralization was initiated near physiological conditions (pH 7.4, 37 °C), by injecting a solution containing Ca^{2+} ions and α-glycerol phosphate, the enzyme substrate, into the QCM-D cells. For both systems, the frequency appreciably decreases then saturates after a certain time to reach the asymptotic shifts (Figure 2A,B). This indicates the successful enzyme-assisted mineralization of the multilayers. Support of this conclusion is given in Figure S3 (Supporting Information), showing that the mineralization does not occur if only Ca^{2+} ions, without α-glycerol phosphate, are injected in the QCM-D cell. An important difference is observed when comparing the asymptotic shifts: −280 Hz for $(PAH/ALP)_5$ and −2000 Hz, $(Col/HA)_3(PAH/ALP)_5$ multilayers, taken at the fifth overtone (Figure 2A,B). The dissipation values recorded after mineralization are also higher for $(Col/HA)_3(PAH/ALP)_5$ multilayers compared to $(PAH/ALP)_5$: 55×10^{-6} and 12×10^{-6}, respectively (Figure 2A,B). These ΔD values may appear surprisingly high, since mineralization is expected to yield a stiff layer, but one should note that the interpretation of the dissipation signal is particularly complex for the studied system. It is worth reminding that, for planar laterally homogeneous films, the dissipation is essentially due to the viscoelastic properties of the layer,[44,45] and the dissipated energy can be described by considering the elastic and viscous compliances. Fitting experimental data requires, however, the need of several parameters, including the film thickness, the real and imaginary parts of compliance, and so on.[46] For spatially heterogeneous films, another mechanism of energy dissipation exists:[47] it is associated with the mechanical properties of the contact zone between the adsorbed "particles" and the surface. Indeed, by combining QCM-D measurements and finite-element method, Johansmann et al. explained the way by which adsorbed soft colloidal particles dissipate the energy. They described, in particular, the role of the nature of their motion at the resonator surface, depending on their size, mode of immobilization, and surface coverage.[47]

An alternative way to examine experimental QCM-D data, when the energy dissipation is not negligible, was proposed by Tellechea et al.,[48] by examining the variation of $\Delta\Gamma/-\Delta f$ ratio, Γ being the half bandwidth at half-maximum and is a parameter equivalent to the dissipation, D. These authors showed that $\Delta\Gamma/-\Delta f$ ratio increases with the object size and decreases with the surface coverage. Following this idea, Figure 2D presents the parametric plots of the ratio $\Delta D/-\Delta f$ as a function of $-\Delta f$ recorded during the mineralization processes of $(PAH/ALP)_5$ (after $t \sim 400$ min) and $(Col/HA)_3(PAH/ALP)_5$ multilayers (after $t \sim 1600$ min). Results show noticeable differences between the studied systems. For $(PAH/ALP)_5$ multilayers, a decrease of $\Delta D/-\Delta f$ ratio with increasing $-\Delta f$ was observed, and the overtones superimpose. This is in accordance with a progressive formation of rigid mineralized particles sticking on the planar surface. The evolution of the $\Delta D/-\Delta f$ versus $-\Delta f$ plots recorded during the mineralization of $(Col/HA)_3(PAH/ALP)_5$ multilayers shows, in contrast, three distinguishable regimes. First, $\Delta D/-\Delta f$ ratio slightly increases for the different overtones. Second, a significant decrease of $\Delta D/-\Delta f$ ratio is observed, showing a linear trend over a large range of frequency shifts. Third, $\Delta D/-\Delta f$ ratio continues to decrease but to a lesser extent and tends to saturate at higher $-\Delta f$ values. The linearity of $\Delta D/-\Delta f$ ratio versus $-\Delta f$, observed in the second regime, has been observed during the adsorption of liposomes on TiO_2-coated crystal,[48] but in the case of that study, the extrapolations of these linear portions, at different overtones, come together to a frequency-independent intercept that corresponds to a unique Sauerbrey mass. Here, the mineralization of $(Col/HA)_3(PAH/ALP)_5$ multilayers shows, in contrast, that the linear portions were fairly parallel at the different overtones, thus, yielding different intercepts (see Figure 2D). The overtone dispersion, on the one hand, and the existence of three regimes, on the other hand, which are observed during the mineralization of $(Col/HA)_3(PAH/ALP)_5$ multilayers, but not for $(PAH/ALP)_5$, indicate that the mechanism of nucleation/growth of CaP particles is greatly influenced by the presence of the $(Col/HA)_3$ multilayers.

Considering that the mineralization of $(PAH/ALP)_5$ and $(Col/HA)_3(PAH/ALP)_5$ multilayers is a process that leads to the formation of heterogeneous films, particularly at early stages, one can assume that the energy dissipation mainly occurs through two different pathways: (i) dissipation in the adsorbed particles themselves and (ii) dissipation in the surrounding liquid. The first pathway can be reasonably considered as negligible, owing to the stiffness of the mineralized CaP particles. Regarding the dissipation in the aqueous medium, the $\Delta D/-\Delta f$ ratio is expected to increase with the object size and decrease with the surface coverage. Regarding the mineralization of $(Col/HA)_3(PAH/ALP)_5$ multilayers, the first regime may be attributed to the nucleation of few and isolated CaP particles, which rapidly grow, leading to an increase of their size. The second regime is dominated by an increase of the surface coverage due to an extensive nucleation/growth of CaP particles on the whole surface. The dispersion of overtones suggests that the mineralized $(Col/HA)_3(PAH/ALP)_5$ is laterally heterogeneous in terms of particle size and/or surface coverage. Finally, during the third regime, the mineralization is leveled off, and this phenomenon could be associated with (i) kinetic considerations related to the mineralization reaction, (ii) a decrease of the enzymatic activity due to autoinactivation processes, or (iii) the presence of the mineralized layer that may reduce the accessibility of the substrate toward immobilized enzymes.

https://doi.org/10.1021/acs.biomac.1c00565
Biomacromolecules 2021, 22, 3460−3473

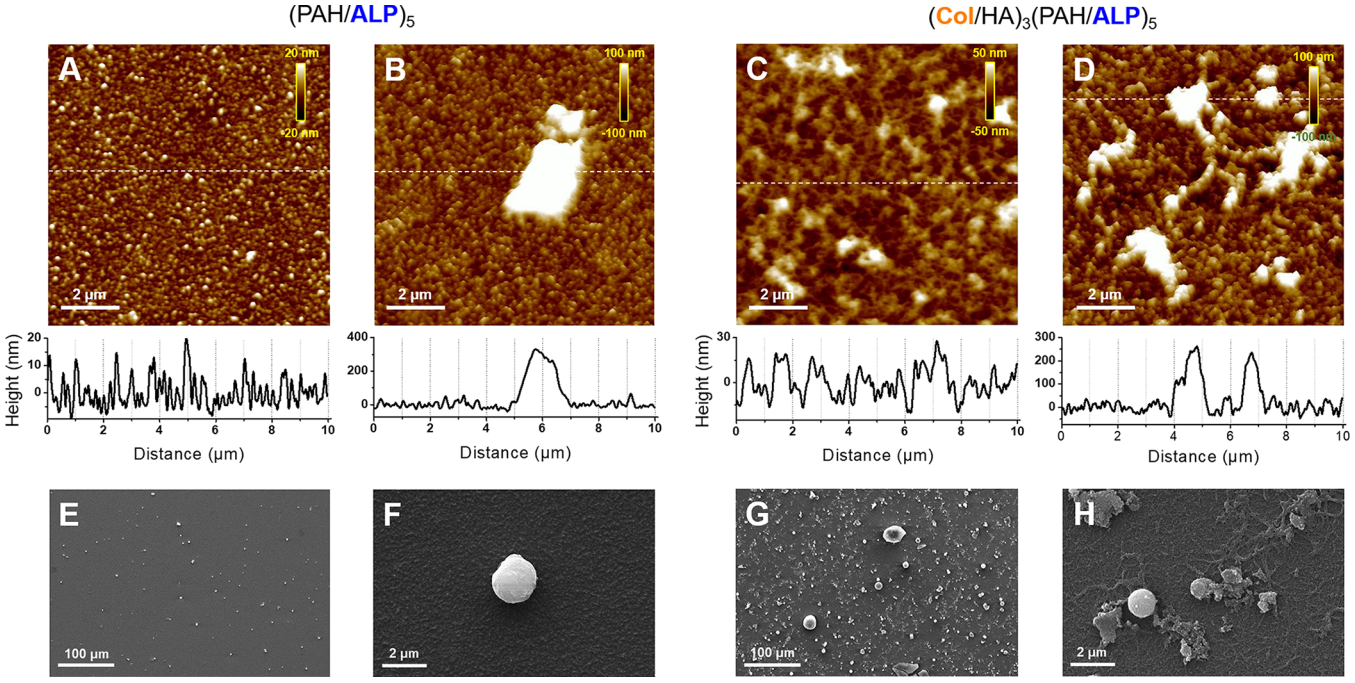

Figure 3. Ex situ characterizations of layer-by-layer assemblies and enzyme-assisted mineralization on planar surface. (A–D) AFM height images recorded on silicon wafers after the buildup of (A) $(PAH/ALP)_5$ and (C) $(Col/HA)_3(PAH/ALP)_5$ multilayers and (B, D) subsequent mineralization (pH 7.4; 37 °C), respectively. Line scans are taken at the locations indicated by dashed lines in the height images. (E–H) SEM images recorded at (E, G) low and (F, H) high magnification on mineralized (E, F) $(PAH/ALP)_5$ and (G, H) $(Col/HA)_3(PAH/ALP)_5$ multilayers.

Ex situ characterizations of $(PAH/ALP)_5$ and $(Col/HA)_3(PAH/ALP)_5$ multilayers prior to and after mineralization brought complementary information, which support QCM-D data. AFM images (Figure 3A,B) show that the mineralization of $(PAH/ALP)_5$ multilayers, after 48 h, leads to the formation of isolated particles, the heights of which are in the range of several hundreds of nanometers (see line scan in Figure 3B), while the topography of the remaining layer did not change markedly. This result was confirmed by recording several AFM images at different locations and on several samples. Unlike $(PAH/ALP)_5$, $(Col/HA)_3(PAH/ALP)_5$ multilayers exhibit a surface network (Figure 3C) that mineralizes more extensively, yielding a mineral phase that seems to form preferentially in the vicinity of the fibrillar nanostructures, presumably made of collagen fibrils (Figure 3D).

SEM images provide an overall view on the particle distribution along the planar surface (Figure 3E–H): only few and isolated particles are visible on the mineralized $(PAH/ALP)_5$ multilayers (Figure 3E,F). By contrast, the mineralization of $(Col/HA)_3(PAH/ALP)_5$ multilayers leads to the extensive formation of larger particles with higher surface coverage (Figure 3G). Furthermore, fibrillar mineralized nanostructures are also visible (Figure 3H), in agreement with AFM findings (Figure 3D). These mineralized particles are clearly visible on the light micrographs used to visualize the sample and the cantilever during AFM imaging (Figure S4, Supporting Information). However, large particles are difficult to image, owing to their heights, which may reach a few micrometers.

3.3. Assemblies and Enzyme-Assisted Mineralization in Nanopores. The incorporation of collagen and enzymes in a multilayered film was also carried out in confinement by means of track-etched membrane used as a template. For this purpose, the LbL assembly of collagen and/or ALP enzymes and their subsequent mineralization were performed following the procedure depicted in Scheme 1. Prior to mineralization, the formation of $(PAH/ALP)_5$ and $(Col/HA)_3(PAH/ALP)_5$ multilayers within nanopores was confirmed by dissolving the template and imaging the liberated nano-objects. TEM micrographs reveal the formation of $(PAH/ALP)_5$, $(Col/HA)_3$, and $(Col/HA)_3(PAH/ALP)_5$ nanotube-like objects by using templates with pore sizes of about 200 and 500 nm (Figure S5, Supporting Information). The walls of the nanotubes are thin due to the low number of bilayers built-up. This leads to their partial breakdown, their twisting, flattening, or shrinking upon the template dissolution. The nanotube walls obtained with the 200 nm pore size template are not easy to identify in the TEM micrographs (Figure S5A–C). By contrast, the hollow structure is clearly visible for nano-objects obtained in a template with 500 nm pore diameter (Figure S5D–F). In this case, the mean thickness of the nanotube wall, computed as the difference between the external and internal diameter of the nanotube, is 25 ± 9 and 33 ± 11 nm for $(PAH/ALP)_5$ and $(Col/HA)_3(PAH/ALP)$, respectively. This increase in the nanotube wall thickness may be attributed to the presence of the cross-linked $(Col/HA)_3$ multilayers.

The mineralization of $(PAH/ALP)_5$ and $(Col/HA)_3(PAH/ALP)_5$ confined multilayers was performed, as for planar surfaces, by incubating the templates in a solution containing Ca^{2+} ions and α-glycerol phosphate for 48 h (Scheme 1). Figure 4 summarizes the variety of nano-objects obtained using templates with pore sizes of 200 and 500 nm after the mineralization of $(PAH/ALP)_5$ and $(Col/HA)_3(PAH/ALP)_5$ multilayers. The mineralization of $(PAH/ALP)_5$ multilayers in 200 nm pore size template leads to the formation of regular nanowires filled with platelet-like structures of hydroxyapatite (HAP), as demonstrated by TEM micrographs (Figure 4A,B),

https://doi.org/10.1021/acs.biomac.1c00565
Biomacromolecules 2021, 22, 3460–3473

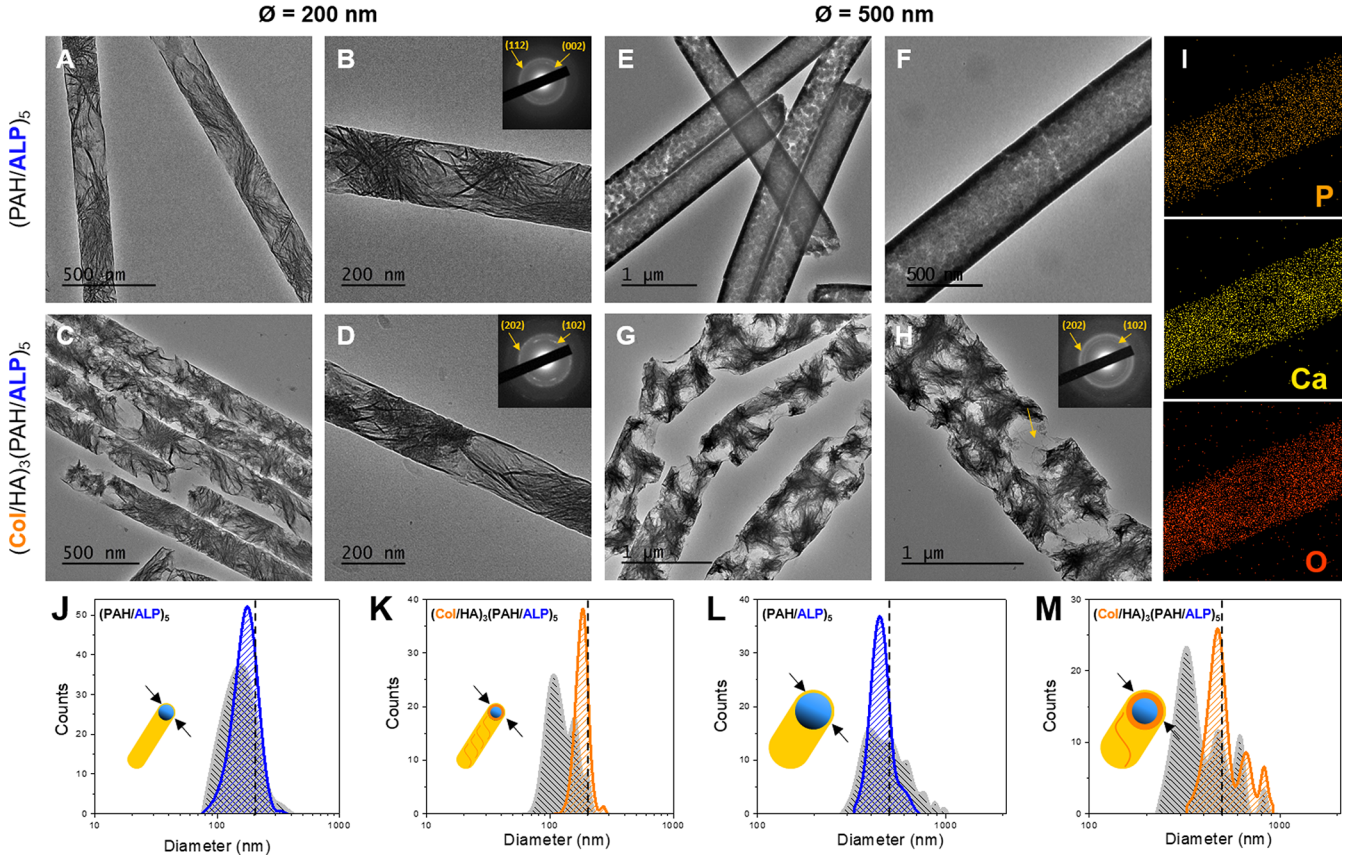

Figure 4. Morphology, crystalline structure, composition, and dimensions from TEM characterizations of nano-objects obtained through the enzyme-assisted mineralization of $(PAH/ALP)_5$ and $(Col/HA)_3(PAH/ALP)_5$ multilayers in 200 and 500 nm pore size template. (A−H) TEM micrographs of (A, B, E, F) $(PAH/ALP)_5$ and (C, D, G, H) $(Col/HA)_3(PAH/ALP)_5$ nano-objects after mineralization for 48 h at pH 7.4 (37 °C) in (A−D) 200 and (E−H) 500 nm pore size template, respectively (SAED patterns in insets). (I) Typical elemental map from a single-nano-object TEM micrograph of phosphorus, calcium, and oxygen recorded with EDX in the STEM mode. (J−M) Size distributions (100 nano-objects) of the diameter of the nanotubes/nanowires prior to (gray) and after mineralization (blue or orange).

in combination with the SAED pattern (Figure 4B, inset). By contrast, in 500 nm pore size template, nano-objects with a hollow structure were obtained with a continuous mineralized wall made of noncrystalline CaP compounds (Figures 4E, F), as confirmed by SAED pattern (not shown).

The mineralized nano-objects obtained with $(Col/HA)_3(PAH/ALP)_5$ multilayers in 200 nm pore size template are similar to those obtained with $(PAH/ALP)_5$, that is, regular nanowires filled with hydroxyapatite platelets (Figure 4C,D). The situation is drastically different in 500 nm pore size template (Figure 4G,H). The morphology of the nano-object obtained with $(Col/HA)_3(PAH/ALP)_5$ multilayers greatly differs from that observed with mineralized $(PAH/ALP)_5$ shown in Figure 4E,F: instead of a hollow structure with a continuous mineralized wall, nanowires filled with both platelet-like structure and fibrillary structures (see arrow in Figure 4H) are observed. The composition of these CaP nanostructures was confirmed by the elemental maps, obtained by EDX in STEM mode, of P, Ca, and O (Figure 4I). Importantly, the mineral phase is made of crystalline hydroxyapatite, as indicated by the SAED patterns (Figure 4H, inset) and confirmed by HRTEM (Figure S6, Supporting Information). The SAED pattern showed the crystallization of hydroxyapatite in the hexagonal lattice by the (002) and (112) diffraction spots (Figure 4H, inset). The inter-reticular distances obtained using the line intensity profiles, extracted from HRTEM micrographs, confirm the crystalline lattice planes of hydroxyapatite with a *d*-spacing of d_{002} = 3.4 Å and d_{300} = 2.7 Å (Figure S6, Supporting Information).

The measurements of the diameter of all the nano-objects obtained with $(PAH/ALP)_5$ and $(Col/HA)_3(PAH/ALP)_5$ multilayers prior to mineralization show large variations in their outside diameters (see gray histograms in Figure 4J−M), due to their possible twisting, flattening, or opening after their extraction from the template. This may be explained by the fact that the walls of the nanotubes are too thin (low number of bilayers, $m = 3$ and $n = 5$) to preserve the mechanical integrity of the whole structure. By contrast, the mineralization of these confined multilayers yields a narrow size distribution with an outside diameter close to the initial diameter of the template nanopore (indicated by dashed lines in Figure 4J−M, see also Table 1). These observations suggest that the mineralization greatly improves the mechanical stability of the nano-objects after their extraction from the template. The case of the mineralized $(Col/HA)_3/(PAH/ALP)_5$ multilayers in the 500 nm pore size template is particularly interesting. Indeed, nano-objects were obtained with a mean external diameter that exceeds, by about 13%, the diameter of the initial nanopores (see Table 1). This observation indicates the ability of these nano-objects to expand after their extraction from the template, suggesting their high flexibility, and may be explained

https://doi.org/10.1021/acs.biomac.1c00565
Biomacromolecules 2021, 22, 3460−3473

Table 1. Characteristics of the Mineralized Nano-Objects (Data from (*) TEM Micrographs; (**) SAED Patterns and HRTEM)

	$(PAH/ALP)_5$		$(Col/HA)_3(PAH/ALP)_5$	
template pore diameter (nm)	200	500	200	500
external diameter* (nm)	184 (26)	465 (61)	185 (21)	558 (142)
morphology*	platelet-like structure	continuous layer	platelet-like structure	platelet-like structure
crystal phase**	HAP	Amorphous	HAP	HAP

by their internal architecture mainly constituted of collagenous filaments interconnected with CaP crystals (Figures 4H 5).

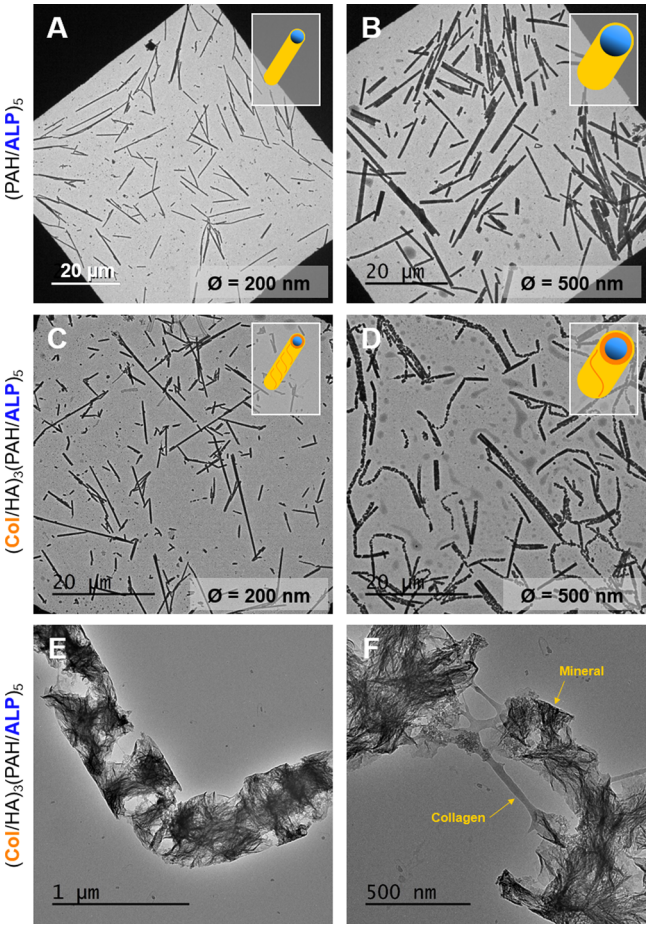

Figure 5. (A–D) TEM micrographs showing the morphologies of the nano-objects obtained through the enzyme-assisted mineralization of (A,B) $(PAH/ALP)_5$ and (C, D) $(Col/HA)_3(PAH/ALP)_5$ multilayers in (A, C) 200 and (B, D) 500 nm pore size template. (E, F) Higher-magnification TEM micrographs showing the typical morphology of $(Col/HA)_3(PAH/ALP)_5$ nano-objects formed using a 500 nm pore size template.

One important issue, connected to the mechanical stability of these nano-objects, is to know whether mineralization occurs uniformly along the length of the nanopore walls. Low-magnification TEM micrographs reveal that all nano-objects are uniformly mineralized along their longitudinal axis, regardless of the multilayers used and the template pore diameter (Figure 5A–D). Some of the nano-object lengths correspond to the overall thickness of the template (ca. 25 μm). This clearly demonstrates the efficiency of the enzymatic approach to control the mineralization process in space, particularly in confined media. Moreover, it is shown, through the distributions of lengths measured on 100 nano-objects for each system (Figure S7, Supporting Information), that the presence of the $(Col/HA)_3$ multilayers has a significant impact on the nano-object lengths. The fraction of nano-objects with a length exceeding 20 μm increases, indeed, from 1% and 0% to 19% and 14% in 200 and 500 nm pore size template, respectively.

These low-magnification TEM micrographs also reveal that mineralized $(PAH/ALP)_5$ multilayers consist of straight lines, regardless of the nano-object length (Figure 5A,B). This feature is also observed for $(Col/HA)_3(PAH/ALP)_5$ multilayers when mineralization was performed in 200 nm pore size template. The straight line-like morphology and the presence of broken mineralized nano-objects suggest that these nanostructures are rather brittle. The characteristics of mineralized $(Col/HA)_3(PAH/ALP)_5$ nano-objects obtained in 500 nm pore size template are, however, different; the morphology shows a dominating presence of bent objects (Figure 5D), suggesting their ability to distort without breaking down.

Figure 5E illustrates the high flexibility of mineralized $(Col/HA)_3(PAH/ALP)_5$ nanotubes, showing their aptitude to distort almost at a right angle. The origin of this outstanding flexibility is revealed in higher-magnification TEM micrograph (Figures 5F). It shows the presence of fibrillary nanostructures, presumably made of collagen, sticking together with hydroxyapatite platelets. The architecture of this composite, confirmed in numerous TEM micrographs, provides to the mineralized nano-objects a better mechanical stability.

Further characterizations regarding the whole morphology of mineralized nano-objects and their mechanical stability are given by SEM images. After their extraction from the template and their collection on a PET membrane, the nano-objects were submitted to several rinsings using an aqueous solution. The mineralization of $(PAH/ALP)_5$ multilayers in a 200 nm pore diameter template shows similar nanostructures, as observed by TEM micrographs: the nano-objects are well-defined and highly anisotropic, but often broken, showing lengths of a few μm, rarely exceeding 10 μm (Figure 6A). In 500 nm pore diameter template, the nano-objects are mostly broken and only a few of them preserved a fairly stable structure (Figure 6B). Their brittleness can be seen through the tubular structure, which exhibits broken areas (Figure 6B, inset).

In contrast, the mineralization of collagen-based multilayers $(Col/HA)_3(PAH/ALP)_5$ in the nanoporous templates produces nano-objects with different characteristics that deserve particular attention. First, their amount after extraction from the template, collection, and further washing is significantly higher compared to mineralized $(PAH/ALP)_5$ nano-objects (Figure 6C,D). Second, their lengths are considerably larger, reaching in most cases about 25 μm, that is, the thickness of the template. This confirms the pivotal role of $(Col/HA)_3$ multilayers to preserve the structures of these mineralized composites and to improve their mechanical stability. Third, the surface topography of these nano-objects is mostly rough and exhibits a high degree of porosity (Figure 6E,F). This characteristic, more pronounced with a 500 nm pore diameter template (Figure 6F), is in agreement with the heterogeneous

https://doi.org/10.1021/acs.biomac.1c00565
Biomacromolecules 2021, 22, 3460–3473

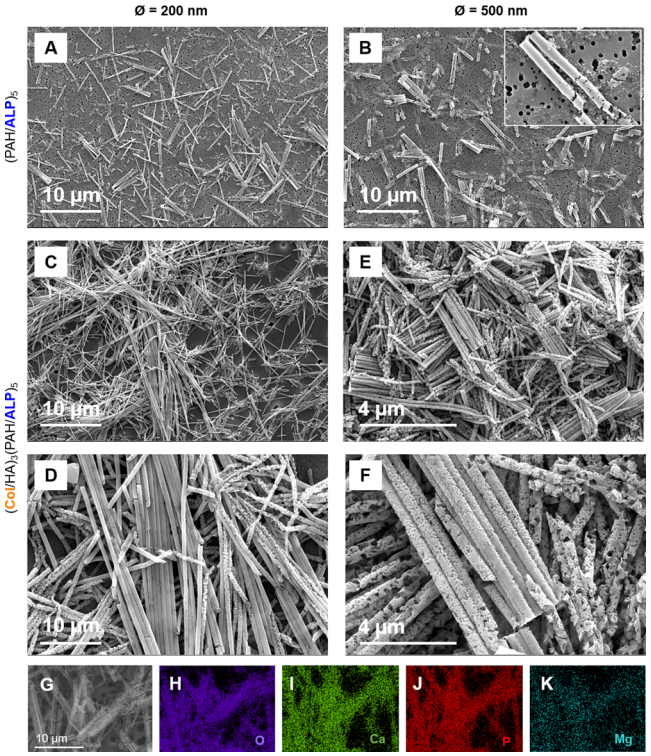

Figure 6. Morphology and composition, from SEM/EDX characterizations, of nano-objects obtained through the enzyme-assisted mineralization of $(PAH/ALP)_5$ and $(Col/HA)_3(PAH/ALP)_5$ multilayers in 200 and 500 nm pore size template. SEM images of (A, B) $(PAH/ALP)_5$ and (C−F) $(Col/HA)_3(PAH/ALP)_5$ nano-objects after mineralization for 48 h at pH 7.4 (37 °C) in (A, C, D) 200 and (B, E, F) 500 nm pore size templates, respectively. (G) Typical SEM image and the corresponding elemental map, from EDX data, of (H) oxygen, (I) calcium, (J) phosphorus, and (K) magnesium.

morphology observed by TEM, which consists in discrete mineralized particles interconnected with fibrillary nanostructures (see arrow in Figure 4H and Figure 5F).

As can be seen on the elemental maps obtained from EDX (Figures 4I and 6G−J), the calcium phosphate elements are well distributed among the samples. In addition, the presence of magnesium dispersed evenly all over the particles can also be observed (Figure 5K). This element comes from the Mg^{2+} counterion of the enzyme substrate, the α-glycerol phosphate magnesium salt hydrate. In a previous study performed in homogeneous solution,[28] XPS measurements provided evidence of the presence of magnesium ions in the surface of CaP particles.

The combination of TEM and SEM observations shows that the incorporation of $(Col/HA)_3$ multilayers, in addition to their influence on the mineralization process, provides more stability to the mineralized nano-objects by maintaining the mineralized particles in a soft network. The presence of collagen-based multilayers provides, indeed, high flexibility to the mineralized nano-objects, thus, preventing their breakdown. This effect is more pronounced in 500 nm pore diameter template, probably because the amount of adsorbed collagen within nanopores is higher compared to 200 nm pore diameter template, as suggested in TEM micrographs (Figure S5C,D,F).

3.4. General Discussion. Through the various systems investigated in this work, the usefulness of immobilizing ALP enzymes on solid surfaces within macromolecular assemblies is displayed. As described in our previous work,[29] releasing phosphate ions in situ through immobilized enzymes is an efficient way to initiate the mineralization at the vicinity of the solid/liquid interface. To take advantage of this feature, in this work, the effects of two complementary levers have been highlighted: the effect of collagen-based multilayers and the role of the confinement. On the one hand, the influence of the Col/HA multilayers on the CaP mineralization is clearly observed by QCM-D and AFM. These experiments conducted on planar surface provide a clear picture regarding the process of mineralization when collagen and enzymes are coassembled in a nanostructured film. The configuration adopted in the present study is, in fact, different from the procedures broadly reported in the literature, for which collagen fibrils are mineralized in the presence of CaP ion precursors without enzymes.[10,11,16,49−51] Indeed, the analysis of the data reported in Figure 2D shows, in particular, that the mineralization process is utterly different with and without the Col/HA multilayers. Without this collagen-based undercoat, the nucleation and growth of particles are limited to the formation of a few isolated rigid particles, which seem to strongly adhere to the planar surface, as suggested by the progressive stiffening of the mineralized layer. With the Col/HA undercoat, on the contrary, a disparate nucleation on the surface is observed. This can result from the presence of the collagen that favors the formation of mineral. AFM images reveal the preferential presence of the mineral phase in the vicinity of collagen fibrillar structures (Figure 3D,H). A complementary experiment was performed where collagen was dispersed homogeneously in solution, as well as the enzyme, its substrate, and Ca^{2+} ions at pH 7.4 and 37 °C. TEM micrographs (Figure S8, Supporting Information) show that, in the solution, crystallized particles are also obtained after 48 h whereas they are still amorphous, or poorly crystalline, after 24 h. Similar experiments performed with PAH instead of collagen have previously shown to yield only amorphous particles.[28] This is in agreement with the literature,[52,53] showing that collagen proteins may guide the mineralization through the formation of crystalline phases, most probably by modifying the surface energy of the solid with which it interacts, as suggested by TEM micrographs (Figure S8). This explains why CaP particles preferentially form on and remain attached to collagen fibrils.

On the other hand, the confinement plays also an obvious role on the morphology of the minerals that are formed during the studied process. In a previous study, we showed that the fraction of nano-objects made of HAP crystals decreases to the detriment of those made of amorphous mineralized structures when increasing the nanopore diameter of the template from 200 to 500 nm.[29] Here, we show that the presence of Col/HA multilayers disturbs the mineralization-confinement balance: crystalline HAP particles are formed, independently of the degree of confinement. Accordingly, two ways of controlling the crystallinity of the mineral formed through the enzymatic-assisted mineralization are proposed. In particular, the incorporation of collagen into the multilayer is shown to be an efficient way to supplement the lack of confinement of the system. Indeed, in the 500 nm pore size template, the confinement alone cannot trigger the mineralization of a crystallized phase whereas, when combined with the incorporation of collagen, HAP crystal phase is clearly formed (see Table 1). Deciphering the exact role(s) that collagen plays in the mineralization process in confinement is a challenge.

https://doi.org/10.1021/acs.biomac.1c00565
Biomacromolecules 2021, 22, 3460−3473

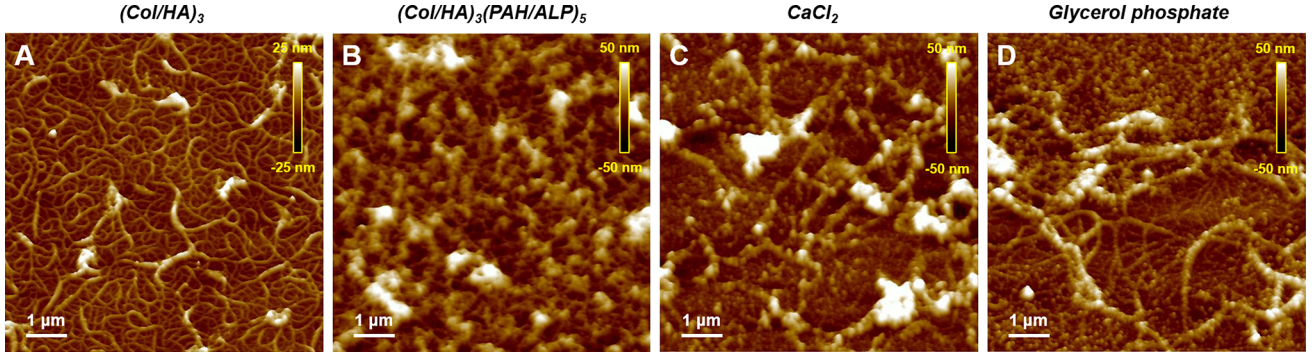

Figure 7. AFM height images recorded on silicon wafers after the buildup of (A) $(Col/HA)_3$ and (B) $(Col/HA)_3(PAH/ALP)_5$; (C) as such and further immersed for 24 h in aqueous solution (pH 7.4 ; 37 °C) containing (C) $CaCl_2$ (11.4 mM) or (D) α-glycerol phosphate (7 mM).

Collagen may, indeed, direct HAP crystallization, in the adsorbed state, similarly to what is observed in homogeneous phase (see Figure S8, Supporting Information). Furthermore, collagen could also play a geometric role on the confinement conditions. Indeed, when collagen molecules (triple-helix) adsorb onto solid surfaces, it has been shown that they adopt a conformation that favors their self-assembly into fibrillary nanostructures and, in many situations near physiological conditions, they interact with the surface through few residues while segments protrude in the solution.[54,55] Besides, the formation of fibrils has also been observed even when collagen is embedded in polyelectrolyte multilayers.[38] In the present study, AFM images recorded on $(Col/HA)_3$ multilayers, after cross-linking, show the presence of well-defined fibrils (Figure 7A), which becomes invisible after the subsequent deposition of $(PAH/ALP)_5$ multilayers (Figure 7B). However, when immersed in an aqueous solution (pH 7.4; 37 °C) containing either Ca^{2+} ions (Figure 7C) or the enzyme substrate (Figure 7D), fibrillary nanostructures reappear clearly. This phenomenon may be due to the interdiffusion of the (bio)-macromolecules and their mobility at the interface in the studied conditions, which, also, favor their swelling. The above findings support the mechanism depicted in Figure 8, describing the mineralization in 500 nm pore size template. Without collagen-based multilayers, the mineralization is comparable to the one observed on the planar surfaces, yielding amorphous CaP particles that grow extensively to form continuous layer (see Figure 4F), suggesting that the confinement effect is not significant in that case for this pore size. In contrast, in the presence of collagen and hyaluronic acid, the confinement of the mineralization area may be enhanced in particular by the collagen fibrils, which protrude in the pore center, their swelling being favored by the mineralization conditions (pH 7.4 ; 37 °C).

In addition to its role in the mineralization process, the incorporation of collagen into the nanotube walls is shown to provide new and interesting mechanical properties to the mineralized nano-objects (Figure 6). Indeed, nanotubes including collagen display a hybrid structure responsible for an increased flexibility (Figure 5E,F) that will be measured in further studies.

To sum up, these objects can easily be tuned through the variability of the templates that can be used, and the versatility of the composition of the LbL assembly that allows the incorporation of various components of interest. Owing to these characteristics, the nano-objects developed here could meet the requirements of numerous biological applications,

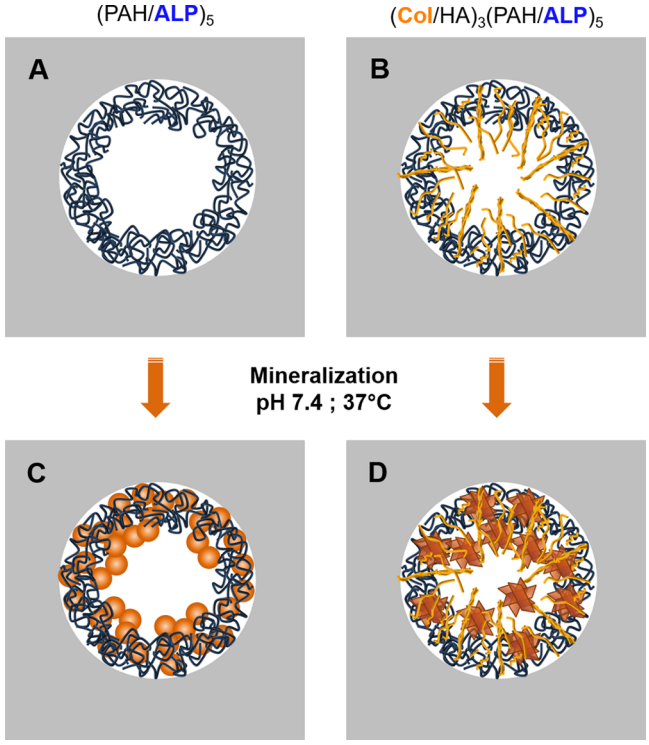

Figure 8. Schematic representation depicting the enzyme-assisted mineralization process in confinement. (A, C) $(PAH/ALP)_5$ and (B, D) $(Col/HA)_3(PAH/ALP)_5$ multilayers (A, B) prior to and (C, D) after mineralization in nanopores (ø = 500 nm). The mineralization of $(PAH/ALP)_5$ multilayer (A) leads to the formation of spheroid amorphous CaP particles (C), which grow to yield a continuously mineralized layer along the nanopore wall, while keeping a hollow structure (see Figure 4F). In the presence of Col/HA multilayer, the swelling of the film is more pronounced and collagen fibrils protrude to the pore center (B). The mineralization of $(Col/HA)_3(PAH/ALP)_5$ multilayer leads to the formation of HAP crystals stacked onto each other and interconnected with collagen fibrillary nanostructures (see Figure 4H).

and are particularly relevant for the control of cell-material interaction. The procedure described in this study does not lead, however, to an intrafibrillar mineralization that would be required to achieve the outstanding mechanical properties of native hard mineralized tissues.[56]

In addition to their outstanding hybrid bio-organic/inorganic nature, the properties of these nano-objects can be easily tuned for more specific applications: the outer and inner

https://doi.org/10.1021/acs.biomac.1c00565
Biomacromolecules 2021, 22, 3460−3473

surfaces can be differentially (bio)-chemically functionalized thanks to the versatility of the LbL technique. This offers the possibility of loading the inside of nanotubes with specific compounds that may be released (e.g., growth and differentiation factors), while conveying biochemical features at the outer surface that may interact with cell receptors.

4. CONCLUSION

In the present paper, we combined (i) the sequential layer-by-layer (LbL) assembly method, (ii) the enzyme-assisted mineralization, and (iii) the template-based synthesis to produce highly ordered hybrid mineralized nano-objects. This biomineralization-inspired approach provides a favorable environment to control CaP nucleation and growth in confinement. Indeed, by coassembling type I collagen and alkaline phosphatase enzymes in a multilayered film within nanopores, we showed the potential of this method to produce mineralized nano-objects. It allowed to tune their features, including their morphology, chemical composition, crystallinity, and mechanical stability. Interestingly, results showed that collagen multilayers play a pivotal role in the mineralization process in confinement. Using the enzyme-assisted mineralization, the fraction of crystalline nano-objects was shown to increase when decreasing the diameter of nanopores. By contrast, the presence of collagen in the multilayered film led to the formation of crystalline hydroxyapatite, independently of the degrees of confinement tested in this study. This suggests that the incorporation of collagen is an efficient way to supplement the lack of confinement. The approach described in this work offers a powerful way for the design of materials mimicking mineralized extracellular matrices in terms of composition, structure, and biomechanical requirements.

■ ASSOCIATED CONTENT

Supporting Information

The Supporting Information is available free of charge at https://pubs.acs.org/doi/10.1021/acs.biomac.1c00565.

Enzymatic activity; QCM-D monitoring of layer-by-layer assemblies; TEM micrographs of nonmineralized nanotubes; and HR-TEM micrographs of the mineral phase (PDF)

■ AUTHOR INFORMATION

Corresponding Author

Jessem Landoulsi − *Laboratoire de Biomécanique and Bioingénierie, CNRS, Université de Technologie de Compiègne, F-60205 Compiègne Cedex, France; Sorbonne Université, CNRS, Laboratoire de Réactivité de Surface, F-75005 Paris, France;* orcid.org/0000-0003-2394-4437; Email: jessem.landoulsi@sorbonne-universite.fr

Authors

Elodie Colaço − *Laboratoire de Biomécanique and Bioingénierie, CNRS, Université de Technologie de Compiègne, F-60205 Compiègne Cedex, France*

Clément Guibert − *Sorbonne Université, CNRS, Laboratoire de Réactivité de Surface, F-75005 Paris, France*

Jihye Lee − *Sorbonne Université, CNRS, Laboratoire de Réactivité de Surface, F-75005 Paris, France*

Emmanuel Maisonhaute − *Sorbonne Université, CNRS, Laboratoire Interfaces et Systèmes Electrochimiques, F-75005 Paris, France;* orcid.org/0000-0001-6337-7436

Dalil Brouri − *Sorbonne Université, CNRS, Laboratoire de Réactivité de Surface, F-75005 Paris, France*

Christine Dupont-Gillain − *Institute of Condensed Matter and Nanosciences, Bio & Soft Matter, Université Catholique de Louvain, 1348 Louvain-la-Neuve, Belgium;* orcid.org/0000-0002-6153-4044

Karim El Kirat − *Laboratoire de Biomécanique and Bioingénierie, CNRS, Université de Technologie de Compiègne, F-60205 Compiègne Cedex, France*

Sophie Demoustier-Champagne − *Institute of Condensed Matter and Nanosciences, Bio & Soft Matter, Université Catholique de Louvain, 1348 Louvain-la-Neuve, Belgium;* orcid.org/0000-0003-3045-6060

Complete contact information is available at: https://pubs.acs.org/10.1021/acs.biomac.1c00565

Notes

The authors declare no competing financial interest.

■ ACKNOWLEDGMENTS

The authors acknowledge Frédéric Nadaud (SAPC, UTC) and Sandra Casale (LRS, Sorbonne Université) for SEM/EDX analyses, the financial support provided by CNRS (INC − Emergence) and the Belgian Fund for Scientific Research (FRS-F.N.R.S-PDR program).

■ REFERENCES

(1) Frantz, C.; Stewart, K. M.; Weaver, V. M. The extracellular matrix at a glance. *J. Cell Sci.* **2010**, *123* (24), 4195−4200.

(2) Bonnans, C.; Chou, J.; Werb, Z. Remodelling the extracellular matrix in development and disease. *Nat. Rev. Mol. Cell Biol.* **2014**, *15* (12), 786−801.

(3) Hussey, G. S.; Dziki, J. L.; Badylak, S. F. Extracellular matrix-based materials for regenerative medicine. *Nat. Rev. Mater.* **2018**, *3* (7), 159−173.

(4) Reznikov, N.; Bilton, M.; Lari, L.; Stevens, M. M.; Kröger, R. Fractal-like hierarchical organization of bone begins at the nanoscale. *Science* **2018**, *360* (6388), eaao2189.

(5) Mendoza-Palomares, C.; Ferrand, A.; Facca, S.; Fioretti, F.; Ladam, G.; Kuchler-Bopp, S.; Regnier, T.; Mainard, D.; Benkirane-Jessel, N. Smart Hybrid Materials Equipped by Nanoreservoirs of Therapeutics. *ACS Nano* **2012**, *6* (1), 483−490.

(6) Kim, S.; Ku, S. H.; Lim, S. Y.; Kim, J. H.; Park, C. B. Graphene−Biomineral Hybrid Materials. *Adv. Mater.* **2011**, *23* (17), 2009−2014.

(7) Rauner, N.; Meuris, M.; Zoric, M.; Tiller, J. C. Enzymatic mineralization generates ultrastiff and tough hydrogels with tunable mechanics. *Nature* **2017**, *543* (7645), 407−410.

(8) Zhang, W.; Liao, S. S.; Cui, F. Z. Hierarchical Self-Assembly of Nano-Fibrils in Mineralized Collagen. *Chem. Mater.* **2003**, *15* (16), 3221−3226.

(9) Jee, S.-S.; Thula, T. T.; Gower, L. B. Development of bone-like composites via the polymer-induced liquid-precursor (PILP) process. Part 1: Influence of polymer molecular weight. *Acta Biomater.* **2010**, *6* (9), 3676−3686.

(10) Niu, L.-n.; Jee, S. E.; Jiao, K.; Tonggu, L.; Li, M.; Wang, L.; Yang, Y.-d.; Bian, J.-h.; Breschi, L.; Jang, S. S.; Chen, J.-h.; Pashley, D. H.; Tay, F. R. Collagen intrafibrillar mineralization as a result of the balance between osmotic equilibrium and electroneutrality. *Nat. Mater.* **2017**, *16* (3), 370−378.

(11) Nudelman, F.; Pieterse, K.; George, A.; Bomans, P. H. H.; Friedrich, H.; Brylka, L. J.; Hilbers, P. A. J.; de With, G.; Sommerdijk, N. A. J. M. The role of collagen in bone apatite formation in the

presence of hydroxyapatite nucleation inhibitors. *Nat. Mater.* **2010**, *9* (12), 1004−1009.
(12) Colaço, E.; Brouri, D.; Aissaoui, N.; Cornette, P.; Dupres, V.; Domingos, R. F.; Lambert, J.-F.; Maisonhaute, E.; Kirat, K. E.; Landoulsi, J. Hierarchical Collagen−Hydroxyapatite Nanostructures Designed through Layer-by-Layer Assembly of Crystal-Decorated Fibrils. *Biomacromolecules* **2019**, *20* (12), 4522−4534.
(13) Qi, C.; Musetti, S.; Fu, L.-H.; Zhu, Y.-J.; Huang, L. Biomolecule-assisted green synthesis of nanostructured calcium phosphates and their biomedical applications. *Chem. Soc. Rev.* **2019**, *48* (10), 2698−2737.
(14) Jiao, K.; Niu, L.-N.; Ma, C.-F.; Huang, X.-Q.; Pei, D.-D.; Luo, T.; Huang, Q.; Chen, J.-H.; Tay, F. R. Complementarity and Uncertainty in Intrafibrillar Mineralization of Collagen. *Adv. Funct. Mater.* **2016**, *26* (38), 6858−6875.
(15) Kim, D.; Lee, B.; Thomopoulos, S.; Jun, Y.-S. The role of confined collagen geometry in decreasing nucleation energy barriers to intrafibrillar mineralization. *Nat. Commun.* **2018**, *9* (1), 962.
(16) Song, Q.; Jiao, K.; Tonggu, L.; Wang, L. G.; Zhang, S. L.; Yang, Y. D.; Zhang, L.; Bian, J. H.; Hao, D. X.; Wang, C. Y.; Ma, Y. X.; Arola, D. D.; Breschi, L.; Chen, J. H.; Tay, F. R.; Niu, L. N. Contribution of biomimetic collagen-ligand interaction to intrafibrillar mineralization. *Sci. Adv.* **2019**, *5* (3), eaav9075.
(17) Kaartinen, M. T.; Pirhonen, A.; Linnala-Kankkunen, A.; Mäenpää, P. H. Cross-linking of Osteopontin by Tissue Transglutaminase Increases Its Collagen Binding Properties. *J. Biol. Chem.* **1999**, *274* (3), 1729−1735.
(18) Fujisawa, K.; Kuboki, Y. Affinity of bone sialoprotein and several other bone and dentin acidic proteins to collagen fibrils. *Calcif. Tissue Int.* **1992**, *51* (6), 438−442.
(19) Zeng, M.; Kim, Y.-Y.; Anduix-Canto, C.; Frontera, C.; Laundy, D.; Kapur, N.; Christenson, H. K.; Meldrum, F. C. Confinement generates single-crystal aragonite rods at room temperature. *Proc. Natl. Acad. Sci. U. S. A.* **2018**, *115* (30), 7670−7675.
(20) Xu, Y.; Sommerdijk, N. A. J. M. Aragonite formation in confinements: A step toward understanding polymorph control. *Proc. Natl. Acad. Sci. U. S. A.* **2018**, *115* (34), 8469−8471.
(21) Jiang, Q.; Ward, M. D. Crystallization under nanoscale confinement. *Chem. Soc. Rev.* **2014**, *43* (7), 2066−2079.
(22) Maas, M.; Guo, P.; Keeney, M.; Yang, F.; Hsu, T. M.; Fuller, G. G.; Martin, C. R.; Zare, R. N. Preparation of Mineralized Nanofibers: Collagen Fibrils Containing Calcium Phosphate. *Nano Lett.* **2011**, *11* (3), 1383−1388.
(23) Van Den Bos, T.; Oosting, J.; Everts, V.; Beertsen, W. Mineralization of alkaline phosphatase-complexed collagen implants in the rat in relation to serum inorganic phosphate. *J. Bone Miner. Res.* **1995**, *10* (4), 616−624.
(24) Duman, E.; Şahin Kehribar, E.; Ahan, R. E.; Yuca, E.; Şeker, U. Ö. Ş. Biomineralization of Calcium Phosphate Crystals Controlled by Protein−Protein Interactions. *ACS Biomater. Sci. Eng.* **2019**, *5* (9), 4750−4763.
(25) Shi, W.; Que, Y.; Zhang, X.; Bian, L.; Yu, X.; Tang, X.; Yang, G.; Dai, Y.; Bi, S.; Lv, D.; Weng, Y.; Wu, W.; Zhang, Z.; Lu, X.; Lu, N. Functional tissue-engineered bone-like graft made of a fibrin scaffold and TG2 gene-modified EMSCs for bone defect repair. *NPG Asia Mater.* **2021**, *13* (1), 28.
(26) Gungormus, M.; Branco, M.; Fong, H.; Schneider, J. P.; Tamerler, C.; Sarikaya, M. Self assembled bi-functional peptide hydrogels with biomineralization-directing peptides. *Biomaterials* **2010**, *31* (28), 7266−7274.
(27) Gungormus, M.; Fong, H.; Kim, I. W.; Evans, J. S.; Tamerler, C.; Sarikaya, M. Regulation of in vitro Calcium Phosphate Mineralization by Combinatorially Selected Hydroxyapatite-Binding Peptides. *Biomacromolecules* **2008**, *9* (3), 966−973.
(28) Colaço, E.; Brouri, D.; Méthivier, C.; Valentin, L.; Oudet, F.; El Kirat, K.; Guibert, C.; Landoulsi, J. Calcium phosphate mineralization through homogenous enzymatic catalysis: Investigation of the early stages. *J. Colloid Interface Sci.* **2020**, *565*, 43−54.
(29) Colaço, E.; Lefèvre, D.; Maisonhaute, E.; Brouri, D.; Guibert, C.; Dupont-Gillain, C.; El Kirat, K.; Demoustier-Champagne, S.; Landoulsi, J. Enzyme-assisted mineralization of calcium phosphate: exploring confinement for the design of highly crystalline nano-objects. *Nanoscale* **2020**, *12* (18), 10051−10064.
(30) Golub, E. E. Role of matrix vesicles in biomineralization. *Biochim. Biophys. Acta, Gen. Subj.* **2009**, *1790* (12), 1592−1598.
(31) Anderson, H. C. Matrix vesicles and calcification. *Curr. Rheumatol. Rep.* **2003**, *5* (3), 222−226.
(32) Schneider, A.; Francius, G.; Obeid, R.; Schwinté, P.; Hemmerlé, J.; Frisch, B.; Schaaf, P.; Voegel, J.-C.; Senger, B.; Picart, C. Polyelectrolyte Multilayers with a Tunable Young's Modulus: Influence of Film Stiffness on Cell Adhesion. *Langmuir* **2006**, *22* (3), 1193−1200.
(33) Kumar, M. R.; Merschrod, E. F.; Poduska, K. M. Collagen-Membrane-Induced Calcium Phosphate Electrocrystallization. *Cryst. Growth Des.* **2011**, *11* (1), 26−28.
(34) Harris, J. R.; Soliakov, A.; Lewis, R. J. In vitro fibrillogenesis of collagen type I in varying ionic and pH conditions. *Micron* **2013**, *49*, 60−68.
(35) Li, Y.; Asadi, A.; Monroe, M. R.; Douglas, E. P. pH effects on collagen fibrillogenesis in vitro: Electrostatic interactions and phosphate binding. *Mater. Sci. Eng., C* **2009**, *29* (5), 1643−1649.
(36) UniProt Knowledgebase. https://www.uniprot.org/uniprot/P09487, accessed 12/04/2020.
(37) Grant, G. G. S.; Koktysh, D. S.; Yun, B.; Matts, R. L.; Kotov, N. A. Layer-By-Layer Assembly of Collagen Thin Films: Controlled Thickness and Biocompatibility. *Biomed. Microdevices* **2001**, *3* (4), 301−306.
(38) Zhang, J.; Senger, B.; Vautier, D.; Picart, C.; Schaaf, P.; Voegel, J.-C.; Lavalle, P. Natural polyelectrolyte films based on layer-by layer deposition of collagen and hyaluronic acid. *Biomaterials* **2005**, *26* (16), 3353−3361.
(39) Johansson, J. Å.; Halthur, T.; Herranen, M.; Söderberg, L.; Elofsson, U.; Hilborn, J. Build-up of Collagen and Hyaluronic Acid Polyelectrolyte Multilayers. *Biomacromolecules* **2005**, *6* (3), 1353−1359.
(40) Landoulsi, J.; Roy, C. J.; Dupont-Gillain, C.; Demoustier-Champagne, S. Synthesis of Collagen Nanotubes with Highly Regular Dimensions through Membrane-Templated Layer-by-Layer Assembly. *Biomacromolecules* **2009**, *10* (5), 1021−1024.
(41) Landoulsi, J.; Demoustier-Champagne, S.; Dupont-Gillain, C. Self-assembled multilayers based on native or denatured collagen: mechanism and synthesis of size-controlled nanotubes. *Soft Matter* **2011**, *7* (7), 3337−3347.
(42) Choi, J.; Rubner, M. F. Influence of the Degree of Ionization on Weak Polyelectrolyte Multilayer Assembly. *Macromolecules* **2005**, *38* (1), 116−124.
(43) Richert, L.; Boulmedais, F.; Lavalle, P.; Mutterer, J.; Ferreux, E.; Decher, G.; Schaaf, P.; Voegel, J.-C.; Picart, C. Improvement of Stability and Cell Adhesion Properties of Polyelectrolyte Multilayer Films by Chemical Cross-Linking. *Biomacromolecules* **2004**, *5* (2), 284−294.
(44) Johannsmann, D. Viscoelastic analysis of organic thin films on quartz resonators. *Macromol. Chem. Phys.* **1999**, *200* (3), 501−516.
(45) Voinova, M. V.; Rodahl, M.; Jonson, M.; Kasemo, B. Viscoelastic Acoustic Response of Layered Polymer Films at Fluid-Solid Interfaces: Continuum Mechanics Approach. *Phys. Scr.* **1999**, *59* (5), 391−396.
(46) Johannsmann, D. Viscoelastic, mechanical, and dielectric measurements on complex samples with the quartz crystal microbalance. *Phys. Chem. Chem. Phys.* **2008**, *10* (31), 4516−4534.
(47) Johannsmann, D.; Reviakine, I.; Richter, R. P. Dissipation in Films of Adsorbed Nanospheres Studied by Quartz Crystal Microbalance (QCM). *Anal. Chem.* **2009**, *81* (19), 8167−8176.
(48) Tellechea, E.; Johannsmann, D.; Steinmetz, N. F.; Richter, R. P.; Reviakine, I. Model-Independent Analysis of QCM Data on Colloidal Particle Adsorption. *Langmuir* **2009**, *25* (9), 5177−5184.

https://doi.org/10.1021/acs.biomac.1c00565
Biomacromolecules 2021, 22, 3460−3473

(49) Zhou, Z.; Zhang, L.; Li, J.; Shi, Y.; Wu, Z.; Zheng, H.; Wang, Z.; Zhao, W.; Pan, H.; Wang, Q.; Jin, X.; Zhang, X.; Tang, R.; Fu, B. Polyelectrolyte−calcium complexes as a pre-precursor induce biomimetic mineralization of collagen. *Nanoscale* **2021**, *13* (2), 953−967.
(50) Al-Munajjed, A. A.; Plunkett, N. A.; Gleeson, J. P.; Weber, T.; Jungreuthmayer, C.; Levingstone, T.; Hammer, J.; O'Brien, F. J. Development of a biomimetic collagen-hydroxyapatite scaffold for bone tissue engineering using a SBF immersion technique. *J. Biomed. Mater. Res., Part B* **2009**, *90B* (2), 584−591.
(51) Farzadi, A.; Renner, T.; Calomeni, E. P.; Presley, K. F.; Karn, N.; Lannutti, J.; Dasi, L. P.; Agarwal, G. Modulation of biomimetic mineralization of collagen by soluble ectodomain of discoidin domain receptor 2. *Mater. Sci. Eng., C* **2019**, *104*, 109905.
(52) Habraken, W. J. E. M.; Tao, J.; Brylka, L. J.; Friedrich, H.; Bertinetti, L.; Schenk, A. S.; Verch, A.; Dmitrovic, V.; Bomans, P. H. H.; Frederik, P. M.; Laven, J.; van der Schoot, P.; Aichmayer, B.; de With, G.; DeYoreo, J. J.; Sommerdijk, N. A. J. M. Ion-association complexes unite classical and non-classical theories for the biomimetic nucleation of calcium phosphate. *Nat. Commun.* **2013**, *4* (1), 1507.
(53) Jiang, S.; Jin, W.; Wang, Y.-N.; Pan, H.; Sun, Z.; Tang, R. Effect of the aggregation state of amorphous calcium phosphate on hydroxyapatite nucleation kinetics. *RSC Adv.* **2017**, *7* (41), 25497−25503.
(54) Gurdak, E.; Dupont-Gillain, C. C.; Booth, J.; Roberts, C. J.; Rouxhet, P. G. Resolution of the Vertical and Horizontal Heterogeneity of Adsorbed Collagen Layers by Combination of QCM-D and AFM. *Langmuir* **2005**, *21* (23), 10684−10692.
(55) Beauvais, M.; Degabriel, T.; Aissaoui, N.; Dupres, V.; Colaço, E.; El Kirat, K.; Domingos, R. F.; Brouri, D.; Pradier, C.-M.; Spadavecchia, J.; Landoulsi, J. Supramolecular Self-Assembly and Organization of Collagen at Solid/Liquid Interface: Effect of Spheroid- and Rod-Shaped TiO2 Nanocrystals. *Adv. Mater. Interfaces* **2019**, *6* (14), 1900195.
(56) Nair, A. K.; Gautieri, A.; Buehler, M. J. Role of Intrafibrillar Collagen Mineralization in Defining the Compressive Properties of Nascent Bone. *Biomacromolecules* **2014**, *15* (7), 2494−2500.

https://doi.org/10.1021/acs.biomac.1c00565
Biomacromolecules 2021, 22, 3460−3473